Lawrence Berkeley National Laboratory
LBL Publications

Title
Surface-Sensitive Photon Avalanche Behavior Revealed by Single-Avalanching-Nanoparticle Imaging

Permalink
https://escholarship.org/uc/item/9qz9w9np

Journal
The Journal of Physical Chemistry C, 125(43)

ISSN
1932-7447

Authors
Kwock, Kevin WC
Lee, Changhwan
Teitelboim, Ayelet
et al.

Publication Date
2021-11-04

DOI
10.1021/acs.jpcc.1c07721

Copyright Information

Peer reviewed

Surface-Sensitive Photon Avalanche Behavior Revealed by Single-Avalanching-Nanoparticle Imaging

Kevin W. C. Kwock[1], Changhwan Lee[2], Ayelet Teitelboim[3], Yawei Liu[3,4], Kaiyuan Yao[2], Sardar B. Alam[3,5], Bruce E. Cohen[3,6]*, Emory M. Chan[3,5]*, P. James Schuck[2]*

[1]Department of Electrical Engineering, Columbia University, New York, NY, USA
[2]Department of Mechanical Engineering, Columbia University, New York, NY, USA
[3]The Molecular Foundry, Lawrence Berkeley National Laboratory, Berkeley, CA, USA
[4]State Key Laboratory of Rare Earth Resource Utilization, Changchun Institute of Applied Chemistry, Chinese Academy of Sciences, Changchun, China
[5]Materials Sciences Division, Lawrence Berkeley National Laboratory, Berkeley, CA, USA
[6]Division of Molecular Biophysics and Integrated Bioimaging, Lawrence Berkeley National Laboratory, Berkeley, CA, USA

*e-mail: p.j.schuck@columbia.edu, emchan@lbl.gov, becohen@lbl.gov

Abstract

Avalanching nanoparticles (ANPs) are a new class of lanthanide-based upconverting material demonstrating steep optical nonlinearities with the potential to advance applications ranging from sub-wavelength bioimaging to neuromorphic computing, nanothermometry and pressure transduction. Here, we use single-nanocrystal imaging to uncover design-dependent heterogeneity in ANP threshold intensity (I_{th}). Quantitative comparisons between distributions of I_{th} and ANP shell properties reveal correlations between mean I_{th} values, histogram widths, and nanocrystal shell thickness. Evaluating avalanching behaviors using an established model of shell-dependent surface energy transfer shows that variations in shell thickness – and the resultant energy transfer from surface to environment – are likely the primary contributor to ANP-to-ANP I_{th} heterogeneity. Further, nanocrystals with ~6 nm average shell thickness show I_{th} heterogeneity beyond the extent expected from statistical measurements of shell size and variability using transmission electron microscopy (TEM). These results provide a principal guide for the design and application of ANPs to environmental sensing.

1. Introduction

Upconverting nanoparticles (UCNPs) exhibit a unique collection of nonlinear, programmable, and photostable[1, 2] optical properties that have enabled their integration into a broad range of applications including low-threshold continuous-wave micro- and nano-lasing[3-5], super-resolution imaging[6-8], X-ray detection[9], deep-tissue imaging[10, 11], and sensing [12-14]. The recent demonstration of photon avalanching in specifically engineered UCNPs – termed avalanching nanoparticles (ANPs)[15] – has further expanded the appeal of lanthanide-based nanomaterials, where the combination of extreme nonlinearity and efficient upconversion opens the possibility of new innovations. However, much remains unexplored in these ANP systems, particularly the uniformity of their avalanching behavior, as well as their possible sensitivity to environmental surroundings, design parameters, and nanocrystal heterogeneity[15, 16].

Imaging and spectroscopy at the level of single molecules and nanoparticles has been employed extensively to uncover and investigate heterogeneity within populations of luminescent probes[17]. Inspired by the pioneering work of W.E. Moerner, we herein report on the optical heterogeneity of Tm^{3+}-based ANPs, using power-dependent single-ANP imaging and energy-transfer modeling to reveal its origins. Photon avalanching (PA) behavior is quantified for ANPs with different shell thicknesses and Tm^{3+} content. Using an established model of energy transfer through UCNP shells, we find that variations in shell thickness primarily govern the observed heterogeneity in emission. We show that ANPs with small shell thicknesses are particularly susceptible to these variations due to the effect of surface-sensitive nonradiative relaxation on PA threshold intensity I_{th} combined with the steeply nonlinear influence of PA on emission brightness. For ANPs with average shell size of ~6 nm – thicker than needed for preventing surface energy loss in UCNPs[18] – the distribution of I_{th} values is notably wider than can be explained by the average and standard deviation of shell thicknesses determined by statistical TEM analysis, highlighting a likely dependence of I_{th} on the thinnest region of shell on a given ANP. These results provide key design rules that immediately impact the development of robust ANPs for sensing, photonics and imaging technologies.

2. Methods

2.1 Experimental Methods

Single-ANP samples were prepared by spin-casting 50 µL of 1 nM concentrations of ANPs dispersed in hexane onto #1.5 glass coverslips with registration markers for enabling correlated AFM and optical imaging. ANP samples were characterized with an AFM (Bruker, Dimension FastScan) to distinguish singles from particle aggregates. Luminescence measurements were performed on a customized inverted microscope (based on a Nikon Eclipse Ti-S inverted microscope). The single ANPs were excited with a CW 1,064-nm laser diode through a numerical aperture (NA) = 1.49, 100x immersion-oil objective (Olympus). Samples were placed on a three-dimensional (XYZ) nanoscanning piezo stage (Physik Instrumente, P-545.xR8S Plano) for sample-scanning confocal imaging. The 800 nm emission was collected with the same objective and filtered through 750-nm long-pass (Thorlabs, FELH750) and 850-nm short-pass (Thorlabs, FESH850) optical filters, then directed either onto a single-photon avalanche diode (Micro Photon Device, PDM series) or into a spectrometer equipped with a CCD array detector (Princeton Instrument, ProEM: 1600^2 eXcelon™3) for spectral evaluation.

To measure the power-dependent avalanching behavior of single ANPs, laser diode powers were simultaneously recorded by a Thorlabs power meter (PM100D and S120C) by using a glass coverslip to reflect ~10% of the incoming flux. Average excitation power densities were calculated using measured laser powers and the $1/e^2$ area calculated from the imaged laser spot.

2.2 Nanoparticle Synthesis

$NaY_{1-x}Tm_xF_4$ ANP cores, of various diameters, were synthesizes based on previously reported procedures[14, 15]. For x=0.08 (8% Tm^{3+} doping), YCl_3 (0.92 mmol, 180 mg) and $TmCl_3$ (0.08 mmol, 22 mg) were combined into a 50 ml 3-neck flask, followed by the addition of 6 ml oleic acid (OA) and 14 ml 1-octadecene (ODE). Under vacuum, the solution was stirred while

simultaneously being heated to 100 °C for 1 hr. Afterwards, when the solution has become clear and purged of water and oxygen, sodium oleate (2.5 mmol, 762 mg) and NH_4F (4 mmol, 148 mg) were added to the flask under N_2 condition. Then, the resealed flask was placed under vacuum for 15 min at 100 °C, followed by 3 pump/purge cycles. After, heat was applied to the flask, heating it from 100 °C to 320 °C (temperature ramp rate was 22 °C/min). The temperature was then held at 320 °C for 45 min. Thereafter, the flask was subjected to rapidly cooling to room temperature with a stream of compressed air.
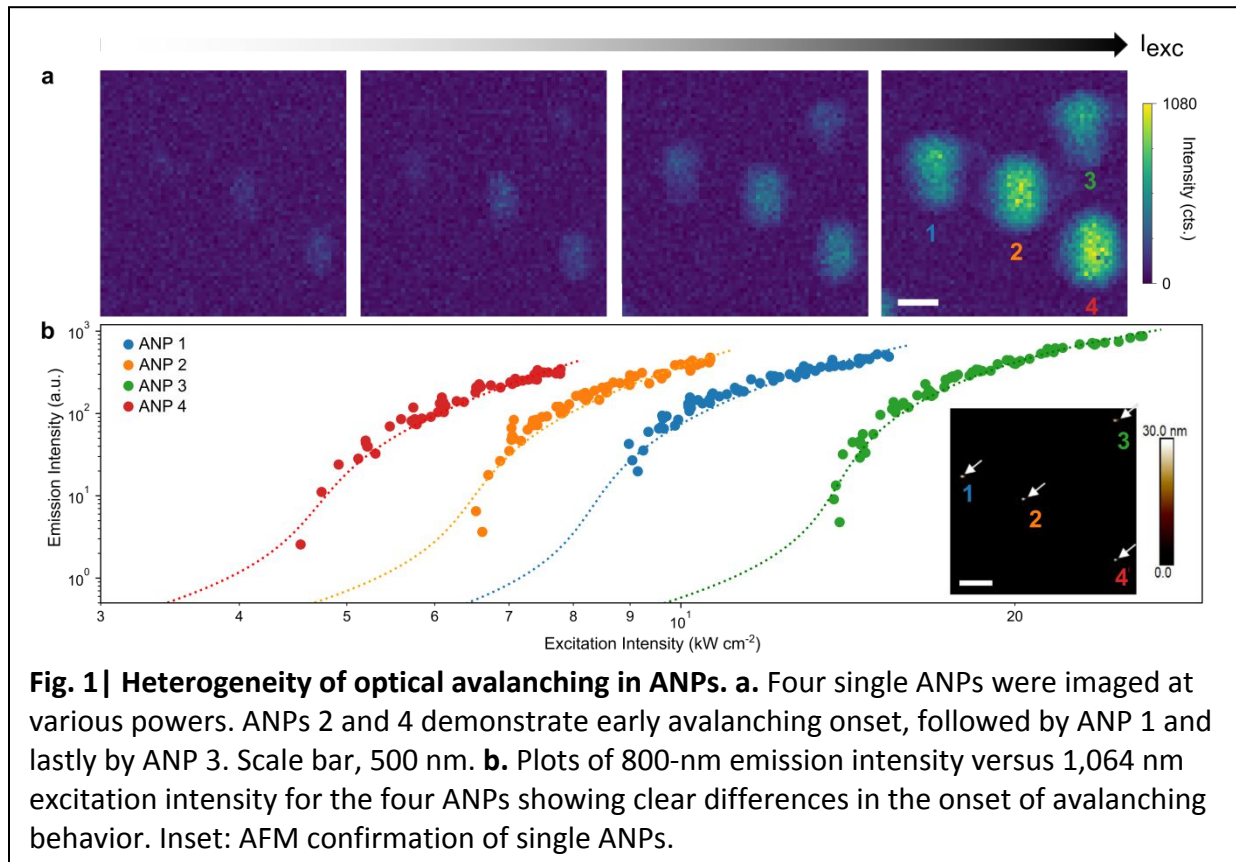
Ethanol was added to the solution so that the nanoparticles could be isolated through centrifugation (2 min at 4000 rpm). The pellet was then suspended in hexanes and centrifuged to remove large and aggregated particles (5 min at 4000 rpm). The nanoparticles were then washed two more times by adding ethanol, isolating by centrifugation, and dissolving the pellet in hexanes. The nanoparticles were stored in hexanes with approximately two drops of oleic acid to prevent particle aggregation.

To perform the shell growth procedure, a 0.1 M stock solution of 20% $GdCl_3$ and 80% YCl_3 was prepared by mixing YCl_3 (2 mmol, 390.5 mg), $GdCl_3$ (0.5 mmol, 131.8 mg), 10 ml OA and 15 ml ODE to a 50 ml 3-neck flask. The solution was stirred and heated to 110 °C under vacuum for 30 min. Then, the flask was filled with N_2 and heated to 180 °C, until the solution became clear and no solids were observed in the flask. Subsequently, the flask was cooled to 100 °C and placed under vacuum for 30 min. A 0.2 M solution of Na-TFA was prepared by combining Na-TFA (4 mmol, 544 mg), 10 ml OA and 10 ml ODE in a flask, under vacuum, at room temperature for 2 hr, ensuring that all chemicals were adequately dissolved. Inside a nitrogen-filled glovebox, an automated nanoparticle synthesis robot (WANDA) was used to grow 3-9 nm $NaY_{0.8}Gd_{0.2}F_4$ shells on ANP cores using a layer-by-layer procedure similar to Levy et. al.[10, 19] Briefly, for a 3 nm shell thickness, 6 mL ODE and 4 mL OA were added to the dried ANP cores and heated to 280 °C at 20 °C/min in the WANDA glove box. The automated protocol alternated between injections of 0.1 M stock solution of 20% gadolinium and 80% Yttrium oleate solution and a 0.2 M Na-TFA stock solution. One injection was performed every 20 minutes for a total of 12 injections (6 injections for each precursor). Following the last injection, each reaction was then annealed at 280 °C for an additional 30 minutes and then cooled rapidly by nitrogen flow. The particles were isolated and purified according to the purification protocol described above.

To characterize the nanoparticles, TEM was performed using a JEOL JEM-2100F field emission transmission electron microscope at an acceleration voltage of 200 kV, FEI Themis 60-300 STEM/TEM operating at an acceleration voltage of 300 kV and Tecnai T20 S-TWIN TEM operating at 200 kV with a LaB6 filament. The nanoparticle size statistics were acquired for approximately 100 nanoparticles using ImageJ software. X-Ray diffraction (XRD) measurement was performed using a Bruker D8 Discover diffractometer with a 35 kV/40 mA Co kα1 source. All $NaYF_4$ nanocrystals were confirmed to have pure hexagonal phase.

3. **Results and Discussion**

3.1 Single-ANP imaging

Fig. 1| Heterogeneity of optical avalanching in ANPs. a. Four single ANPs were imaged at various powers. ANPs 2 and 4 demonstrate early avalanching onset, followed by ANP 1 and lastly by ANP 3. Scale bar, 500 nm. **b.** Plots of 800-nm emission intensity versus 1,064 nm excitation intensity for the four ANPs showing clear differences in the onset of avalanching behavior. Inset: AFM confirmation of single ANPs.

To study the optical heterogeneity between individual ANPs with nominally the same structure, scanning confocal microscopy was performed on single, 8% Tm^{3+} 16 nm/8.5 nm core/shell nanocrystals from the same synthetic batch. Previously, these ANPs were shown to have the lowest average avalanching threshold intensities among the studied designs and an average optical nonlinearity of s=20.8, where emission intensity I_{em} scales with excitation intensity I_{exc} to the *s* power ($I_{em} \propto I_{exc}^{s}$)[15]. By imaging single ANPs at different excitation intensities, ANP-to-ANP variations in the onset of PA (i.e., in the avalanching threshold intensity I_{th}) become immediately evident (Fig. 1). Four single ANPs, confirmed by AFM imaging (Fig. 1b inset), are highlighted. ANPs 2 and 4 demonstrate an earlier avalanching onset compared to the others, showing noticeable emission at ~6.50 kW cm^{-2}. At ~13 kW cm^{-2}, ANP 3 finally begins avalanching as the other particles enter the saturation regime.

Following the imaging, the emission behavior as a function of excitation intensity is measured in greater detail for each ANP (see, e.g., Fig. 1b) by collecting I_{em} while focusing the excitation laser on each ANP, allowing us to quantify I_{th} and relative variations. For the ANPs in Fig. 1, we observe that the PA onset for ANP 3 is approximately 3x larger than for ANP 4, consistent with the imaging data. Because ANP emission is so low when excitation intensity is below I_{th}, we note that for most individual ANPs, the detected signal surpasses the noise floor only after the nanoparticle has been excited beyond its threshold intensity and is fully in the avalanching regime (Fig. 1b).

3.2 Extrapolation of avalanching threshold from DRE model
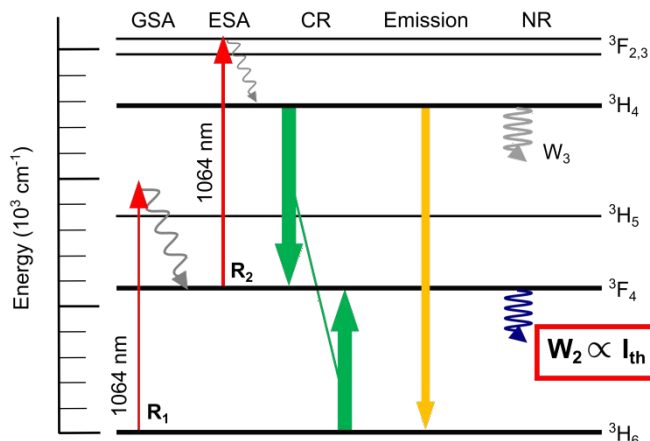
Fig. 2| Energy-level diagram of Tm-based ANPs. Energy-level diagram depicting Tm^{3+} transitions and energy pathways within the ANP. In particular, nonradiative losses to surface ligands and the substrate, captured in $W_{2,NR}$, contribute to the avalanching heterogeneity seen across different single ANPs. When cross-relaxation rates are large, the overall W_2 ($W_{2,NR} + W_{2,R}$) is proportional to I_{th}. R_1 and R_2 represent ground-state and excited-state pumping rates. GSA, ground-state absorption. ESA, excited-state absorption. CR represents cross-relaxation, an energy transfer between Tm^{3+} ions within the ANP. Thicker arrows represent faster rates.
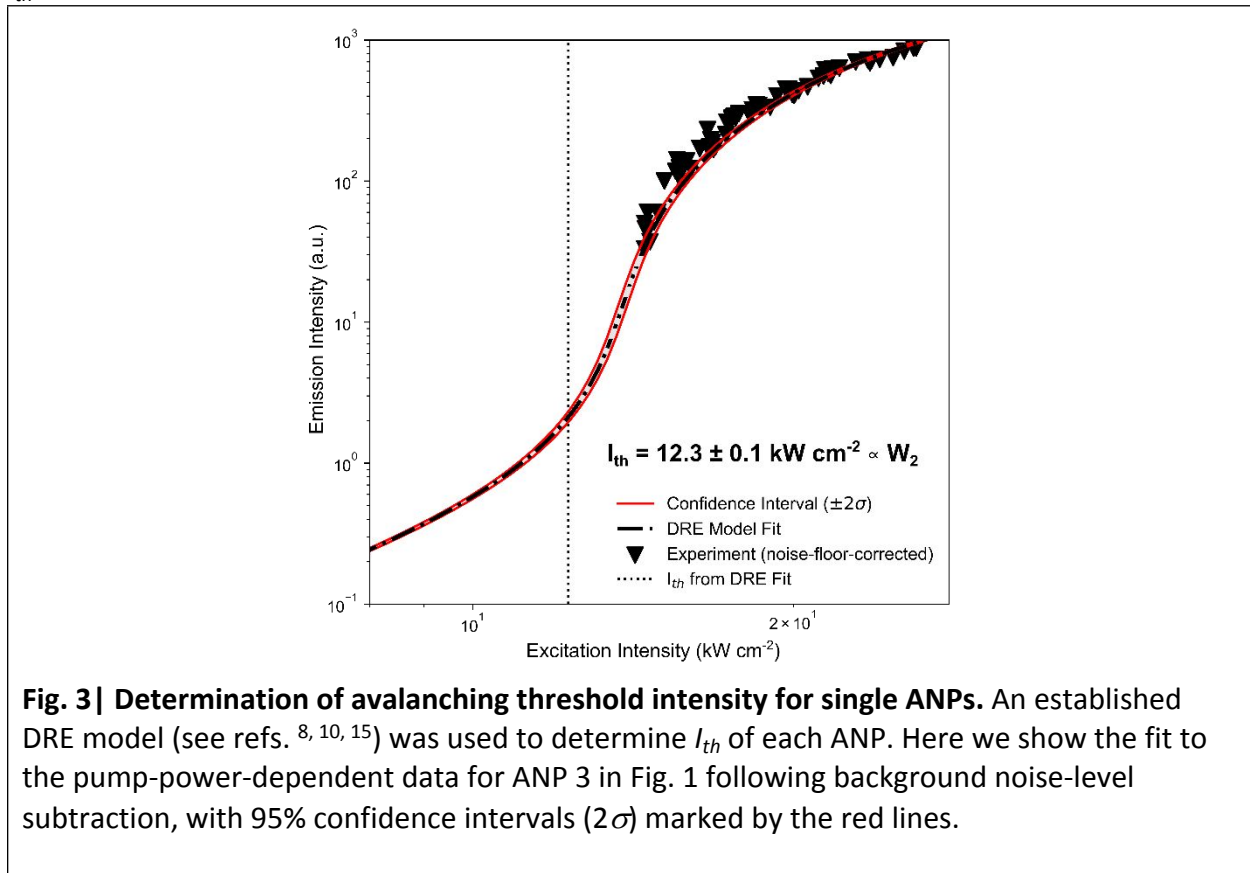
Previous work has shown that a nonlinear differential rate equation (DRE) model of the avalanching process can be used to accurately reproduce the measured PA emission behavior in these ANPs[15, 20]. While the I_{th} for most individual ANPs cannot be observed directly due to the low signal near I_{th}, fitting the measured emission vs. excitation intensity curves using reported DREs from Lee *et. al.* allows us to determine the I_{th} for each particle[15]. In these coupled DREs, the excited-state absorption (ESA) rate $R_2 = \sigma_{ESA}(1064 \text{ nm}) \bullet I_{exc}$, where $\sigma_{ESA}(1064 \text{ nm})$ is the absorption cross-section for the Tm^{3+} ESA transition from the $^3F_4$ state to the $^3F_{2,3}$ levels at $\lambda = 1064$ nm (Fig. 2). In the limit that the cross-relaxation (CR) rate is large compared to W_2 and W_3 (the relaxation rates of the $^3F_4$ and $^3H_4$ states, respectively), which is true for ANPs with Tm^{3+} content $\geq 8\%$[15], the condition for achieving I_{th} is simply given by:

$$R_{2,th} \approx \sigma_{ESA}I_{th} = W_2$$

With $R_{2,th}$ being the excited-state pumping rate at the PA threshold. Specifically, this equation emphasizes that in these ANPs, W_2 is directly proportional to I_{th}.

W_2 consists of radiative ($W_{2,R}$) and nonradiative ($W_{2,NR}$) components. Here, $W_{2,R}$ is assumed to be constant at 83.3 s^{-1}, though we note that local changes in the optical density of states surrounding the ANP can modify this quantity as well[21]. In the DRE model, we varied the $W_{2,NR}$ as a fitting parameter to calculate the total W_2 value and thus the avalanching threshold of each ANP based on its measured I_{em} vs. I_{exc} curve. An example of the fitting, confidence intervals, and extrapolated I_{th} (Fig. 3) shows excellent agreement between the model fit and the

measured data for ANP 3 in Fig. 1, yielding a W_2 value of 383.2 ± 3.7 s^{-1} and corresponding to an I_{th} of 12.3 ± 0.1 kW cm^{-2}.

Fig. 3| Determination of avalanching threshold intensity for single ANPs. An established DRE model (see refs. [8, 10, 15]) was used to determine I_{th} of each ANP. Here we show the fit to the pump-power-dependent data for ANP 3 in Fig. 1 following background noise-level subtraction, with 95% confidence intervals (2σ) marked by the red lines.

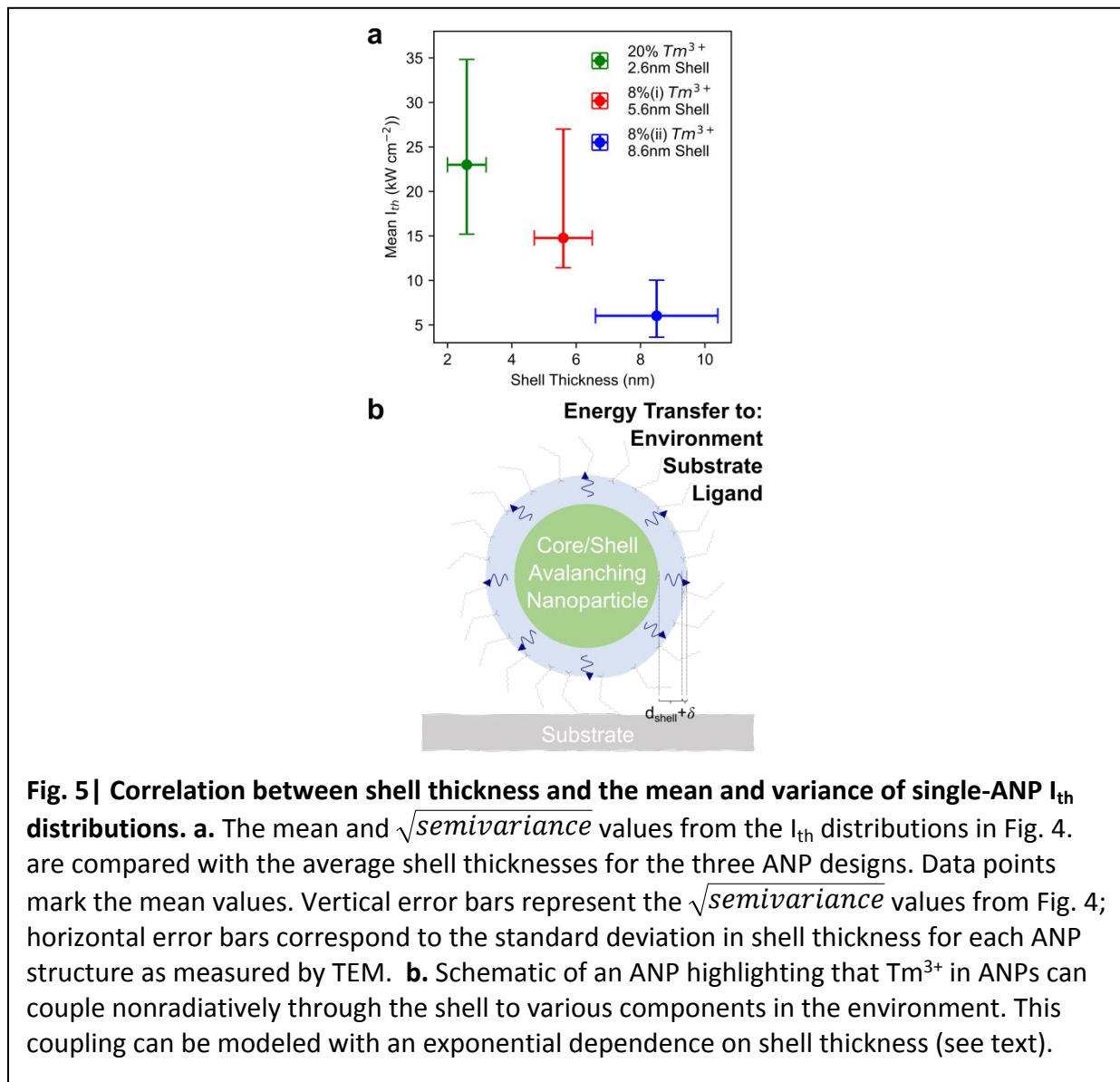### 3.3 Histograms of single-particle avalanching heterogeneity

Distributions of I_{th} values for three different ANP designs were assembled (Fig. 4) by first imaging, then collecting and fitting I_{em} vs. I_{exc} curves for >100 single particles of each design using the procedure described above. The nominal structures for the three core/shell ANP types are: 20% Tm^{3+} 17.4/2.6 nm (core diameter/shell thickness); 8% Tm^{3+} 17.3/5.6 nm; and 8% Tm^{3+} 16/8.5 nm, hereafter denoted as the 20%, 8%(i), and 8%(ii) samples, respectively. The ANPs are slightly prolate in shape (see ref. 15 for details), with the given sizes being an average of the major and minor axes. From the distributions, the mean I_{th} values are found to be 23, 14.8, and 6 kW cm^{-2} for the 20%, 8%(i), and 8%(ii) designs, respectively. The distributions are asymmetric as expected (see below). Semivariances were calculated for each side of the distributions, with square-root values of -7.7/+11.7, -3.3/+12, and -2.4/+4 kW cm^{-2}, respectively (dotted lines in Fig. 4).

Fig. 4| Histograms of single-ANP I_{th} values. a-c. Single-particle avalanching thresholds for ANPs from three different design batches were determined using power-dependent emission measurements combined with DRE modeling. Different degrees of heterogeneity are exhibited for the ANP designs. Three Tm^{3+} doped ANP batches were measured: a) 20% Tm^{3+} (2.6-nm shells), b) 8%(i) Tm^{3+} (5.6-nm shells), and c) 8%(ii) Tm^{3+} (8.5-nm shells). See text for additional structural details. For each measurement, sample sizes exceeded 120 single particles. All distributions are asymmetric, skewed towards higher threshold intensities. The solid lines correspond to the mean values of the histogram data, and the dashed lines correspond to the square root of the calculated semi-variances.

For proper comparison to the ensemble film studies in ref. 15, we note that the excitation intensities reported in this work correspond to the *peak* intensity of the diffraction limited excitation spot, since each particle is much smaller than the excitation spot and care was taken to center the individual ANPs within the laser spot while collecting signal. Meanwhile, for the ANP film measurements, the reported excitation intensities were the *full-width-at-half-maximum* (FWHM) intensity values of the focused excitation beam, since this provides an approximate average intensity felt by the collection of ANPs distributed throughout the focal spot.

Two trends emerge from comparison of the single-ANP I_{th} distributions: 1) the mean threshold intensities and 2) distribution widths both correlate inversely with shell thickness (Fig. 5a data points and vertical error bars). Thicker-shelled particles yield lower I_{th} values and smaller deviations from the mean, highlighting the fact that thicker-shelled particles better passivate the core from nonradiative losses. Based on these trends, we hypothesize that ANP-to-ANP variations in avalanching threshold intensity originate primarily from heterogeneity in passivating shell thickness, and are particularly pronounced for particles with thinner shells. It is known that a major energy loss pathway in Ln-doped nanoparticles is nonradiative surface quenching, where energy is transferred from NIR Ln^{3+} transitions to external excitations (e.g., vibrational modes) at the nanoparticle surface and/or surrounding environment (Fig. 5b) [22-24]. These losses can effectively be suppressed by the addition of optically inert passivating shells, with studies on UCNPs showing that most quenching is eliminated for shells ≥ 6 nm [18, 25, 26]. Within the context of ANPs, this surface quenching directly effects $W_{2,NR}$, which increases as shell thickness decreases.
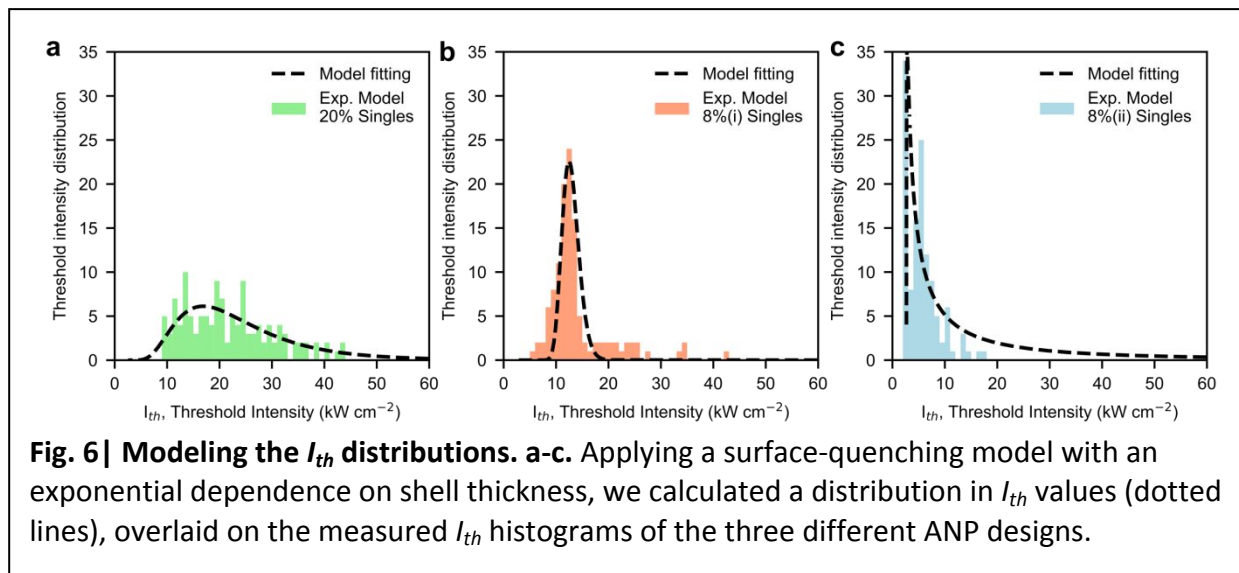
Fig. 5| Correlation between shell thickness and the mean and variance of single-ANP I_{th} distributions. a. The mean and $\sqrt{semivariance}$ values from the I_{th} distributions in Fig. 4. are compared with the average shell thicknesses for the three ANP designs. Data points mark the mean values. Vertical error bars represent the $\sqrt{semivariance}$ values from Fig. 4; horizontal error bars correspond to the standard deviation in shell thickness for each ANP structure as measured by TEM. **b.** Schematic of an ANP highlighting that Tm^{3+} in ANPs can couple nonradiatively through the shell to various components in the environment. This coupling can be modeled with an exponential dependence on shell thickness (see text).

3.4 Modeling single ANP heterogeneity

To test this hypothesis and further understand the effects of shell thickness heterogeneity on avalanching threshold intensity, we utilize the previously established surface energy transfer model from Fischer *et al.* in which they found that the rate of surface quenching can be accurately described using an exponential dependence on shell thickness[18].

$$W_{2,NR}(d_{shell}, \pm \delta) = \Gamma_0 \cdot e^{-\kappa(d_{shell} \pm \delta)} \cdot \frac{(R_{core} + d_{shell} \pm \delta)^2}{R_{core}^2} \tag{1}$$

In Eq. 1, the surface quenching losses are approximated as $W_{2,NR}$ in our DRE model, which is accurate because the nonradiative multiphonon relaxation rate from $^3F_4$ to $^3H_6$ is

Fig. 6| Modeling the I_{th} distributions. a-c. Applying a surface-quenching model with an exponential dependence on shell thickness, we calculated a distribution in I_{th} values (dotted lines), overlaid on the measured I_{th} histograms of the three different ANP designs.

negligible in β-NaYF$_4$ nanocrystal hosts[10]. Here, d_{shell} is the average shell thickness and δ represents the standard deviation in shell thickness for the particles in a given distribution. The surface quenching loss rate of a particle without a shell, I_0, is set to 2380 s^{-1} [18]. For κ, the exponential passivation improvement with shell thickness, we assigned a value of 0.9 nm^{-1}, using the same value from ref. [18] that corresponds to surface energy transfer (ET) for the first-excited-state transition in Er^{3+}, which is similar in energy to the $^3F_4$ transition in Tm^{3+} relevant here (~6450 cm^{-1} and ~5700 cm^{-1}, respectively).

We fit the model to the experimentally measured histograms, setting d_{shell} and δ as adjustable fitting parameters. Fig. 6 shows the results of these fits (dotted lines) overlaid on the histogram data from Fig. 4 for each of the three ANP designs. This analysis allows us to directly compare the d_{shell} and δ values determined by the model with the same quantities measured previously by transmission electron microscopy (TEM) (see Fig. S1 and ref. 15). The comparison displays excellent agreement, thus supporting our hypothesis that variations in shell thickness are the primary contributor to heterogeneity in ANP I_{th}.

Specifically, we find that for the 20% and 8%(ii) ANPs, the model-fitted and TEM-measured values of d_{shell} and δ nearly match within error: For 8%(ii), d_{shell} = 8.7 ± 2.7 nm (model fit, including uncertainty in fitted value) vs. 8.5 nm (TEM); δ = 2.7 ± 1.2 nm (model fit, including uncertainty in fitted value) vs. 1.9 nm (TEM). For 20%, d_{shell} = 2.3 ± 0.1 nm (model fit) vs. 2.6 nm (TEM); δ = 0.7 ± 0.1 nm (model fit) vs. 0.6 nm (TEM). For the 8%(i) ANPs, the fit shows general qualitative agreement with shape of the main peak in the histogram, but there is less quantitative correspondence. In this case, the measured histogram leads to a smaller estimated d_{shell} value in the model than what is observed on average with TEM (3.04 ± 0.02 nm (model fit) vs. 5.6 nm (TEM)). The same is true for δ (δ = 0.22 ± 0.02 nm (model fit) vs. 0.9 nm (TEM)).

The discrepancies are likely evidence of other existing heterogeneities at the level of individual ANPs. Specifically, this can include shell asymmetries surrounding single particles,

which are difficult to measure with TEM due to damage considerations. Here, average shell diameters from TEM are found indirectly, by subtracting average core diameters from average core/shell diameters. Thus, actual shell thickness variations on any given ANP are unknown. Considering this limitation, the discrepancy between the model fit and the average TEM values can be explained if I_{th} depends more on the thinnest part of the ANP shell rather than the average shell thickness. This dependence on minimum shell thickness is consistent with known energy migration distances within Ln-doped nanoparticles and with our observed distribution widths for the 8%(i) and 8%(ii) ANP batches. Specifically, the 8%(i) particles with average shell thickness of 5.6 nm are much more likely to have sub-5-nm surface-loss pathways than are the 8%(ii) particles, with average shell thickness of 8.5 nm. For the latter, we indeed observe that emission properties are relatively homogeneous, since even when accounting for the TEM-measured standard deviation in shell thickness of 1.9 nm, the thinnest shell regions will largely remain ≥ 6 nm.

More generally, these results highlight the potential application of ANPs as sensitive reporters of their local environment. For thinner shelled particles, the relatively large degree of heterogeneity observed here makes clear that any process capable of modifying W_2 – e.g., any radiative or nonradiative coupling to the broad Tm^{3+} $^3F_4$ state – will change I_{th} and thus profoundly impact particle brightness because of the steeply nonlinear nature of PA[15, 16]. This can include local changes in C-H and O-H bond densities, whose vibrational overtones energetically overlap the $^3F_4$ transition, as well as changes in proximity to molecules, materials or structures with electronic transitions or modified optical density of states in the shortwave infrared regime. The results also provide guidance for design considerations when engineering ANPs as sensors, showing that shell thicknesses should be greater than κ^{-1} but less than 6 nm. Design optimization for each application will involve balancing environmental ET and sensitivity, which is heightened for thin shells, and lower I_{th} requirements, with I_{th} minimized for thicker shells.

4. Conclusion

Through single-particle imaging and interrogation methods, this study reveals varying degrees of heterogeneity in photon avalanching threshold intensities for three different designs of ANPs. By quantifying the distributions of I_{th} values and evaluating the histogram data using a surface ET model, we show that variations in particle shell thickness are primarily responsible for the observed I_{th} heterogeneity. The correlations between the optical heterogeneity of ANPs to variations in shell thickness established here provide potential strategies for synthesizing particles designed for environmental sensing, where the PA process is expected to add an additional level of sensitivity compared to existing UCNPs that exploit the standard energy-transfer upconversion mechanism.
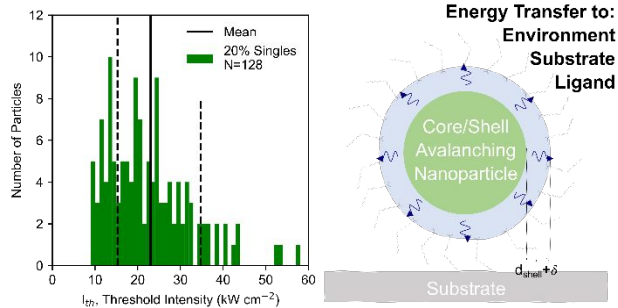
Supporting Information

TEM microscopy and statistics of 20%, 8%(i), and 8%(ii) single ANPs; relationship between I_{th} and W_2; determining the histogram statistics for upper-bound avalanching thresholds of ANPs; perturbative FRET model fit to histogram data; histogram statistical prediction with perturbative FRET model and the surface quenching model; correlation between AFM microscopy of single ANPs with I_{th}

1
2
3
4
5
6
7
8
9
10
11
12
13
14
15
16
17
18
19
20
21
22
23
24
25
26
27
28
29
30
31
32
33
34
35
36
37
38
39
40
41
42
43
44
45
46
47
48
49
50
51
52
53
54
55
56
57
58
59
60

Acknowledgements

TOC Graphic

References

1. Wu, S.; Han, G.; Milliron, D. J.; Aloni, S.; Altoe, V.; Talapin, D. V.; Cohen, B. E.; Schuck, P. J., Non-blinking and photostable upconverted luminescence from single lanthanide-doped nanocrystals. *Proceedings of the National Academy of Sciences* **2009,** *106* (27), 10917-10921.

2. Park, Y. I.; Kim, J. H.; Lee, K. T.; Jeon, K. S.; Na, H. B.; Yu, J. H.; Kim, H. M.; Lee, N.; Choi, S. H.; Baik, S. I., Nonblinking and nonbleaching upconverting nanoparticles as an optical imaging nanoprobe and T1 magnetic resonance imaging contrast agent. *Advanced Materials* **2009,** *21* (44), 4467-4471.

3. Fernandez-Bravo, A.; Wang, D.; Barnard, E. S.; Teitelboim, A.; Tajon, C.; Guan, J.; Schatz, G. C.; Cohen, B. E.; Chan, E. M.; Schuck, P. J., Ultralow-threshold, continuous-wave upconverting lasing from subwavelength plasmons. *Nature Materials* **2019,** *18* (11), 1172-1176.

4. Fernandez-Bravo, A.; Yao, K.; Barnard, E. S.; Borys, N. J.; Levy, E. S.; Tian, B.; Tajon, C. A.; Moretti, L.; Altoe, M. V.; Aloni, S., Continuous-wave upconverting nanoparticle microlasers. *Nature Nanotechnology* **2018,** *13* (7), 572-577.

5. Liu, Y.; Teitelboim, A.; Fernandez-Bravo, A.; Yao, K.; Altoe, M. V. P.; Aloni, S.; Zhang, C.; Cohen, B. E.; Schuck, P. J.; Chan, E. M., Controlled assembly of upconverting nanoparticles for low-threshold microlasers and their imaging in scattering media. *ACS Nano* **2020,** *14* (2), 1508-1519.

6. Chen, C.; Wang, F.; Wen, S.; Su, Q. P.; Wu, M. C.; Liu, Y.; Wang, B.; Li, D.; Shan, X.; Kianinia, M., Multi-photon near-infrared emission saturation nanoscopy using upconversion nanoparticles. *Nature Communications* **2018,** *9* (1), 1-6.

7. Denkova, D.; Ploschner, M.; Das, M.; Parker, L. M.; Zheng, X.; Lu, Y.; Orth, A.; Packer, N. H.; Piper, J. A., 3D sub-diffraction imaging in a conventional confocal configuration by exploiting super-linear emitters. *Nature Communications* **2019,** *10* (1), 1-12.

8. Liu, Y.; Lu, Y.; Yang, X.; Zheng, X.; Wen, S.; Wang, F.; Vidal, X.; Zhao, J.; Liu, D.; Zhou, Z., Amplified stimulated emission in upconversion nanoparticles for super-resolution nanoscopy. *Nature* **2017,** *543* (7644), 229-233.

9. Ou, X.; Qin, X.; Huang, B.; Zan, J.; Wu, Q.; Hong, Z.; Xie, L.; Bian, H.; Yi, Z.; Chen, X., High-resolution X-ray luminescence extension imaging. *Nature* **2021,** *590* (7846), 410-415.

10. Levy, E. S.; Tajon, C. A.; Bischof, T. S.; Iafrati, J.; Fernandez-Bravo, A.; Garfield, D. J.; Chamanzar, M.; Maharbiz, M. M.; Sohal, V. S.; Schuck, P. J., Energy-looping nanoparticles: harnessing excited-state absorption for deep-tissue imaging. *ACS Nano* **2016,** *10* (9), 8423-8433.

11. Chamanzar, M.; Garfield, D. J.; Iafrati, J.; Chan, E. M.; Sohal, V.; Cohen, B. E.; Schuck, P. J.; Maharbiz, M. M., Upconverting nanoparticle micro-lightbulbs designed for deep tissue optical stimulation and imaging. *Biomedical Optics Express* **2018,** *9* (9), 4359-4371.

12. Garfield, D. J.; Borys, N. J.; Hamed, S. M.; Torquato, N. A.; Tajon, C. A.; Tian, B.; Shevitski, B.; Barnard, E. S.; Suh, Y. D.; Aloni, S., Enrichment of molecular antenna triplets amplifies upconverting nanoparticle emission. *Nature Photonics* **2018,** *12* (7), 402-407.

13. Tajon, C. A.; Yang, H.; Tian, B.; Tian, Y.; Ercius, P.; Schuck, P. J.; Chan, E. M.; Cohen, B. E., Photostable and efficient upconverting nanocrystal-based chemical sensors. *Optical Materials* **2018,** *84*, 345-353.

14. Ostrowski, A. D.; Chan, E. M.; Gargas, D. J.; Katz, E. M.; Han, G.; Schuck, P. J.; Milliron, D. J.; Cohen, B. E., Controlled synthesis and single-particle imaging of bright, sub-10 nm lanthanide-doped upconverting nanocrystals. *ACS Nano* **2012,** *6* (3), 2686-2692.

15.   Lee, C.; Xu, E. Z.; Liu, Y.; Teitelboim, A.; Yao, K.; Fernandez-Bravo, A.; Kotulska, A. M.; Nam, S. H.; Suh, Y. D.; Bednarkiewicz, A., Giant nonlinear optical responses from photon-avalanching nanoparticles. *Nature* **2021,** *589* (7841), 230-235.

16.   Bednarkiewicz, A.; Chan, E. M.; Kotulska, A.; Marciniak, L.; Prorok, K., Photon avalanche in lanthanide doped nanoparticles for biomedical applications: super-resolution imaging. *Nanoscale Horizons* **2019,** *4* (4), 881-889.

17.   Moerner, W., A dozen years of single-molecule spectroscopy in physics, chemistry, and biophysics. *The Journal of Physical Chemistry B* **2002,** *106* (5), 910-927.

18.   Fischer, S.; Bronstein, N. D.; Swabeck, J. K.; Chan, E. M.; Alivisatos, A. P., Precise tuning of surface quenching for luminescence enhancement in core–shell lanthanide-doped nanocrystals. *Nano Letters* **2016,** *16* (11), 7241-7247.

19.   Chan, E. M.; Xu, C.; Mao, A. W.; Han, G.; Owen, J. S.; Cohen, B. E.; Milliron, D. J., Reproducible, high-throughput synthesis of colloidal nanocrystals for optimization in multidimensional parameter space. *Nano Letters* **2010,** *10* (5), 1874-1885.

20.   Guy, S.; Joubert, M.; Jacquier, B., Photon avalanche and the mean-field approximation. *Physical Review B* **1997,** *55* (13), 8240.

21.   Villanueva-Delgado, P.; Biner, D.; Krämer, K., Judd–Ofelt analysis of β-NaGdF$_4$: Yb^{3+}, Tm^{3+} and β-NaGdF$_4$: Er^{3+} single crystals. *Journal of Luminescence* **2017,** *189*, 84-90.

22.   Boyer, J.-C.; Van Veggel, F. C., Absolute quantum yield measurements of colloidal NaYF$_4$: Er^{3+}, Yb^{3+} upconverting nanoparticles. *Nanoscale* **2010,** *2* (8), 1417-1419.

23.   Hossan, M. Y.; Hor, A.; Luu, Q.; Smith, S. J.; May, P. S.; Berry, M. T., Explaining the nanoscale effect in the upconversion dynamics of β-NaYF$_4$: Yb^{3+}, Er^{3+} core and core–shell nanocrystals. *The Journal of Physical Chemistry C* **2017,** *121* (30), 16592-16606.

24.   Wen, S.; Zhou, J.; Zheng, K.; Bednarkiewicz, A.; Liu, X.; Jin, D., Advances in highly doped upconversion nanoparticles. *Nature Communications* **2018,** *9* (1), 1-12.

25.   Johnson, N. J.; He, S.; Diao, S.; Chan, E. M.; Dai, H.; Almutairi, A., Direct evidence for coupled surface and concentration quenching dynamics in lanthanide-doped nanocrystals. *Journal of the American Chemical Society* **2017,** *139* (8), 3275-3282.

26.   Tian, B.; Fernandez-Bravo, A.; Najafiaghdam, H.; Torquato, N. A.; Altoe, M. V. P.; Teitelboim, A.; Tajon, C. A.; Tian, Y.; Borys, N. J.; Barnard, E. S., Low irradiance multiphoton imaging with alloyed lanthanide nanocrystals. *Nature Communications* **2018,** *9* (1), 1-8.

1
2
3
4
5
6
7
8
9
10
11
12
13
14
15
16
17
18
19
20
21
22
23
24
25
26
27
28
29
30
31
32
33
34
35
36
37
38
39
40
41
42
43
44
45
46
47
48
49
50
51
52
53
54
55
56
57
58
59
60